arXiv:1703.06820v1 [physics.flu-dyn] 20 Mar 2017

# Deformations of a pre-stretched and lubricated finite elastic sheet

**Evgeniy Boyko, Amir D. Gat† and Moran Bercovici‡**

Faculty of Mechanical Engineering, Technion - Israel Institute of Technology, Haifa, Israel

(Received 2017)

The interaction of an elastic sheet with a thin viscous film appears in a wide range of natural phenomena and can be utilized as an actuation mechanism for surface deformations, applicable to microfluidics, optics, and soft robotics. Implementation of such configurations inherently takes place over finite domains and often requires pre-stretching of the sheet. Under the assumptions of strong pre-stretching and small deformations of the lubricated elastic sheet, we derive Green's functions describing the deformation in a finite domain due to external forces acting either directly on the sheet or through the fluid, accounting for both bending and stretching effects. Using these Green's functions we provide a closed-form solution for the case of a square-shaped actuation and present the effect of pre-stretching on the dynamics of the deformation. We further study the dependence of the deformation magnitude on the spatial wavenumber, revealing its effect on the transition between stretching and bending dominant regimes. Finally, we present the effect of spatial discretization of the forcing (representing practical actuation) on the achievable resolution.

## 1. Introduction

Elastohydrodynamic interaction between an elastic substrate and a thin liquid film is of interest in the study of various natural processes, such as passage of air flow in the lungs (Grotberg & Jensen 2004) and geological formation of laccoliths (Michaut 2011), as well as in the dynamic control of elastic structures for applications in soft robotics, adaptable optics and reconfigurable microfluidics (Whitesides *et al.* 2001; Chronis *et al.* 2003; Kim *et al.* 2013). In particular, the case of viscous fluid confined between an elastic sheet and a rigid surface has been extensively studied in the context of viscous peeling (Hosoi & Mahadevan 2004; Lister *et al.* 2013; Hewitt *et al.* 2015), suppression of viscous fingering instabilities (Pihler-Puzović *et al.* 2012, 2013; Al-Housseiny *et al.* 2013; Pihler-Puzović *et al.* 2014), impact mitigation (Tulchinsky & Gat 2016), elastohydrodynamic wakes (Arutkin *et al.* 2016), and application of non-uniform lubrication flows to obtain complex deformation patterns of elastic plates (Rubin *et al.* 2017).

Previous studies of viscous-elastic dynamics, including our own work on deformation of elastic surfaces (Rubin *et al.* 2017), considered a non-pre-stretched infinite elastic plate and employed either linear Kirchhoff-Love bending model or non-linear Foppl-von Karman equations (Timoshenko & Woinkowsky-Krieger 1987), which account for both bending and internal stretching, to describe deformations depending on relative magnitude of deformation as compared to thickness of elastic sheet. An exception is recent work of Kodio *et al.* (2017), who studied the dynamics of wrinkling of an elastic beam lying on a viscous film resulting from externally applied compressive force.

For applications involving thin elastic sheets (e.g. a $\sim$10 $\mu m$ polymer sheet, or a $\sim$1

† Email address for correspondence: amirgat@technion.ac.il
‡ Email address for correspondence: mberco@technion.ac.il

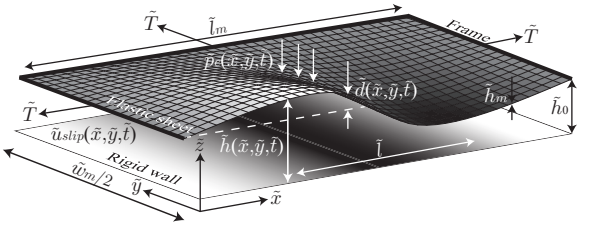


FIGURE 1. Schematic illustration showing the centerline cross-section of the examined configuration. A thin viscous fluid layer of initial thickness $\tilde{h}_0$, is confined between a rigid surface and a pre-stretched elastic sheet supported at its boundaries. Non-uniform and time-varying slip velocity $\tilde{\boldsymbol{u}}_{slip}(\tilde{x},\tilde{y},\tilde{t})$ and external pressure $\tilde{p}_e(\tilde{x},\tilde{y},\tilde{t})$ drive the viscous-elastic interaction and create the deformation field $\tilde{d}(\tilde{x},\tilde{y},\tilde{t})$.

$\mu m$ biological membrane) it is difficult to implement configurations without introducing pre-stretching of the sheets. Thus, pure bending model cannot be expected to provide adequate prediction. Furthermore, any natural or engineered system involves finite boundaries which strongly affect the deformation dynamics. In this work, we address for the first time these two aspects and examine the viscous-elastic dynamics of a pre-stretched elastic sheet on a finite domain (e.g. a frame holding the sheet). We present the equations governing the deformation field, provide their scaling, and derive new Green's functions, accounting for both bending and stretching on a finite domain, for forces applied either directly to the sheet or through the fluid. Focusing on electro-osmotic actuation, we present a closed-form solution for the practical case of a square-shaped actuation region within a finite domain. We present the effect of pre-stretching on the steady-state deformation pattern and magnitude, and examine the timescales for development of pressure and deformation. Using a Fourier decomposition, we further study the tradeoff between spatial resolution, and the achievable amplitude, and show its different scaling in tension versus bending dominant regimes. Finally, we examine the effect of spatial discretization of the forcing (representing, e.g., actuation electrodes) on the resulting deformation.

## 2. Problem formulation and governing equations

We study the viscous-elastic dynamics of a viscous fluid of density $\tilde{\rho}$ and viscosity $\tilde{\mu}$ confined between a rigid surface and a pre-stretched elastic sheet of length $\tilde{l}_m$, width $\tilde{w}_m$, thickness $\tilde{h}_m$, Young's modulus $\tilde{E}_Y$, and Poisson ratio $\nu$, as shown in figure 1. We denote dimensional variables by tildes, normalized variables without tildes and characteristic values by an asterisk superscript. We employ a Cartesian coordinate system $(\tilde{x},\tilde{y},\tilde{z})$, and adopt the $\parallel$ and $\perp$ subscripts to denote parallel and perpendicular directions to the $\tilde{x}-\tilde{y}$ plane, respectively.

The fluid velocity is $\tilde{\boldsymbol{u}} = \left(\tilde{\boldsymbol{u}}_{\parallel},\tilde{\boldsymbol{u}}_{\perp}\right) = (\tilde{u},\tilde{v},\tilde{w})$ and fluid pressure is $\tilde{p}$. The total gap between the plates is $\tilde{h}(\tilde{x},\tilde{y},\tilde{t}) = \tilde{h}_0 + \tilde{d}(\tilde{x},\tilde{y},\tilde{t})$, where $\tilde{t}$ is time and $\tilde{h}_0$ is the initial gap. The deformation field $\tilde{d}(\tilde{x},\tilde{y},\tilde{t})$ is induced either due to an external pressure $\tilde{p}_e(\tilde{x},\tilde{y},\tilde{t})$, acting directly on the elastic sheet, or by a non-uniform slip velocity $\tilde{\boldsymbol{u}}_{slip}(\tilde{x},\tilde{y},\tilde{t})$ on the rigid surface, which exerts a force on the fluid and varies over a characteristic length scale $\tilde{l}$ in the $\tilde{x}-\tilde{y}$ plane. The characteristic velocities in the $\tilde{x}-\tilde{y}$ plane and $\hat{\boldsymbol{z}}$ direction are respectively $\tilde{u}^*$ and $\tilde{w}^*$, and the characteristic pressure, deformation and time are respectively denoted as $\tilde{p}^*$, $\tilde{d}^*$, and $\tilde{t}^*$.

We assume that the solid's inertia is negligible and focus on the case of a strongly pre-stretched elastic sheet with isotropic tension $\tilde{T}$, assumed to be much larger than

any internal tension, $\tilde{T}_{in}$, forming in the system. From scaling of a Foppl-von Karman equation that couples the spatial variations in internal tension to Gaussian curvature (Howell *et al.* 2009, p. 176), we find $\tilde{T}_{in} \sim (\tilde{d}^*/\tilde{l})^2 \tilde{E}_Y \tilde{h}_m$, and define

$$\alpha = \frac{\tilde{T}_{in}}{\tilde{T}} = \left(\frac{\tilde{d}^*}{\tilde{l}}\right)^2 \frac{\tilde{E}_Y \tilde{h}_m}{\tilde{T}} \ll 1. \tag{2.1}$$

Based on the assumptions mentioned above, the deformations of the elastic sheet are described by (see Timoshenko & Woinkowsky-Krieger 1987; Howell *et al.* 2009)

$$\tilde{p} = \tilde{B}\tilde{\nabla}_{\parallel}^4 \tilde{d} - \tilde{T}\tilde{\nabla}_{\parallel}^2 \tilde{d} + \tilde{p}_e, \tag{2.2}$$

where $\tilde{\boldsymbol{\nabla}}_{\parallel} = (\partial/\partial\tilde{x}, \partial/\partial\tilde{y})$ is the two-dimensional gradient and $\tilde{B} = \tilde{E}_Y \tilde{h}_m^3/12(1-\nu^2)$ is the bending stiffness. Equation (2.2) is supplemented by the boundary conditions

$$\tilde{d} = 0, \quad \frac{\partial^2 \tilde{d}}{\partial n^2} = 0, \quad \frac{\partial^4 \tilde{d}}{\partial n^4} = 0 \quad \text{at} \quad \Omega, \tag{2.3}$$

and the initial condition $\tilde{d}(\tilde{x}, \tilde{y}, \tilde{t} = 0) = 0$. The first two conditions correspond to no deflection and no moment at the boundary $\Omega$, whereas the last condition is obtained from (2.2) by requiring the fluidic and external pressures are equal at the boundaries, $\tilde{p} = \tilde{p}_e$. We defined $\Omega$ hereafter as $\tilde{x} = 0$, $\tilde{l}_m$ and $\tilde{y} = 0$, $\tilde{w}_m$, having a normal $\hat{\boldsymbol{n}}$.

Scaling by the characteristic dimensions, we define the following normalized quantities: $(x, y, z) = (\tilde{x}/\tilde{l}, \tilde{y}/\tilde{l}, \tilde{z}/\tilde{h}_0)$, $(u, v, w) = (\tilde{u}/\tilde{u}^*, \tilde{v}/\tilde{u}^*, \tilde{w}/\tilde{w}^*)$, $p = \tilde{p}/\tilde{p}^*$, $t = \tilde{t}/\tilde{t}^*$, $d = \tilde{d}/\tilde{d}^*$ and $h = \tilde{h}/\tilde{h}_0$. When scaling (2.2), we introduce a dimensionless number $\lambda$ that represents the relative contribution of bending and stretching to the deformation of the elastic sheet

$$\lambda \equiv \frac{\text{Bending}}{\text{Stretching}} = \frac{\tilde{B}}{\tilde{T}\tilde{l}^2} = \frac{1}{12(1-\nu^2)} \frac{\tilde{E}_Y \tilde{h}_m}{\tilde{T}} \left(\frac{\tilde{h}_m}{\tilde{l}}\right)^2 = \frac{\alpha}{12(1-\nu^2)} \left(\frac{\tilde{h}_m}{\tilde{d}^*}\right)^2, \tag{2.4}$$

where the last equality in (2.4) stems from the condition (2.1), resulting in

$$\frac{\tilde{d}^*}{\tilde{l}} = \frac{\tilde{p}^* \tilde{l}}{\tilde{T}} \quad \text{and} \quad p = \lambda \nabla_{\parallel}^4 d - \nabla_{\parallel}^2 d + p_e. \tag{2.5}$$

We restrict our analysis to shallow geometries, to negligible fluidic inertia, represented by small Womersley and reduced Reynolds numbers, and to small elastic deformations,

$$\epsilon = \frac{\tilde{h}_0}{\tilde{l}} \ll 1, \quad Wo = \frac{\tilde{\rho}\tilde{h}_0^2}{\tilde{\mu}\tilde{t}^*} \ll 1, \quad \epsilon Re = \epsilon \frac{\tilde{\rho}\tilde{u}^* \tilde{h}_0}{\tilde{\mu}} \ll 1, \quad \frac{\tilde{d}^*}{\tilde{h}_0} \ll 1. \tag{2.6}$$

Based on (2.6), the fluid motion is governed by the lubrication equations (Leal 2007)

$$\tilde{\boldsymbol{\nabla}} \cdot \tilde{\boldsymbol{u}} = 0, \quad \tilde{\boldsymbol{\nabla}}_{\parallel} \tilde{p} = \tilde{\mu} \frac{\partial^2 \tilde{\boldsymbol{u}}_{\parallel}}{\partial \tilde{z}^2}, \quad \frac{\partial \tilde{p}}{\partial \tilde{z}} = 0. \tag{2.7}$$

The fluid is subjected to the slip and the no-penetration boundary conditions on the bottom surface. Horizontal motion of the elastic sheet is negligible at the small deformation limit, implying the no-slip and the no-penetration boundary conditions along it,

$$\left(\tilde{\boldsymbol{u}}_{\parallel}, \tilde{\boldsymbol{u}}_{\perp}\right)|_{\tilde{z}=0} = \left(\tilde{\boldsymbol{u}}_{slip}(\tilde{x}, \tilde{y}, \tilde{t}), 0\right), \quad \left(\tilde{\boldsymbol{u}}_{\parallel}, \tilde{\boldsymbol{u}}_{\perp}\right)|_{\tilde{z}=\tilde{h}} = \left(\boldsymbol{0}, \frac{\partial \tilde{d}}{\partial \tilde{t}}\right). \tag{2.8}$$

From order of magnitude analysis of (2.7) and (2.8) we obtain $\tilde{w}^* = \epsilon \tilde{u}^*$, $\tilde{p}^* = 12\tilde{\mu}\tilde{u}^*/\epsilon^2 \tilde{l}$, $\tilde{t}^* = \tilde{d}^*/\tilde{w}^* = \tilde{d}^*/\epsilon\tilde{u}^*$ and $Wo = (\tilde{h}_0/\tilde{d}^*)\epsilon Re$. In addition, using (2.5) yields the viscous-elastic time scale $\tilde{t}^* = 12\tilde{\mu}\tilde{l}/\epsilon^3 \tilde{T}$.

Based on this scaling, and following standard lubrication theory, from (2.7) and (2.8) we obtain the normalized Reynolds equation (Leal 2007, p. 313)

$$\frac{\partial d}{\partial t} - \boldsymbol{\nabla}_{\parallel} \cdot \left[ h^3 \boldsymbol{\nabla}_{\parallel} p - \frac{1}{2} h \boldsymbol{u}_{slip}(x,y) \right] = 0. \tag{2.9}$$

Substituting (2.5) into (2.9), yields the non-linear governing equation

$$\frac{\partial d}{\partial t} - \boldsymbol{\nabla}_{\parallel} \cdot \left[ h^3 \boldsymbol{\nabla}_{\parallel} \left[ \lambda \nabla_{\parallel}^4 d - \nabla_{\parallel}^2 d \right] \right] = -h \boldsymbol{\nabla}_{\parallel} \cdot \boldsymbol{f}_F + \boldsymbol{\nabla}_{\parallel} \cdot \left[ h^3 \boldsymbol{\nabla}_{\parallel} f_E \right]. \tag{2.10}$$

where we define $\boldsymbol{f}_F = f_{Fx}\hat{\boldsymbol{x}} + f_{Fy}\hat{\boldsymbol{y}} = 0.5\boldsymbol{u}_{slip}$ and $f_E = p_e$ as the actuation mechanisms. Subscript $F$ refers to driving force applied to the sheet through pressure in the fluid and subscript $E$ refers to driving force applied on the elastic sheet.

Assuming small elastic deformations, $\tilde{d}^* \ll \tilde{h}_0$, yields the linearized viscous-elastic governing equation in terms of deformation accounting for both bending and pre-stretching (Kodio *et al.* 2017), and containing a source term that depends on the external forces

$$\frac{\partial d}{\partial t} - \lambda \nabla_{\parallel}^6 d + \nabla_{\parallel}^4 d = -\boldsymbol{\nabla}_{\parallel} \cdot \boldsymbol{f}_F + \nabla_{\parallel}^2 f_E, \tag{2.11}$$

subjected to the boundary conditions (2.3). The corresponding dimensional equation is

$$\frac{\partial \tilde{d}}{\partial \tilde{t}} - \tilde{\boldsymbol{\nabla}}_{\parallel} \cdot \left[ \frac{\tilde{h}_0^3}{12\tilde{\mu}} \tilde{\boldsymbol{\nabla}}_{\parallel} \left[ \tilde{B} \tilde{\nabla}_{\parallel}^4 \tilde{d} - \tilde{T} \tilde{\nabla}_{\parallel}^2 \tilde{d} \right] \right] = -\tilde{h}_0 \tilde{\boldsymbol{\nabla}}_{\parallel} \cdot \tilde{\boldsymbol{f}}_F + \frac{\tilde{h}_0^3}{12\tilde{\mu}} \tilde{\nabla}_{\parallel}^2 \tilde{f}_E. \tag{2.12}$$

## 3. Derivation of Green's functions solutions

Sixth-order diffusion equations are encountered in various problems involving viscous-elastic interactions, such as viscous peeling (Hosoi & Mahadevan 2004), elastohydrodynamic wakes (Arutkin *et al.* 2016) and wrinkles (Kodio *et al.* 2017). However, to the best of our knowledge, the general solution of (2.11) with corresponding finite boundary conditions (2.3) in terms of Green's function has not been presented yet.

The Green's equation for the differential operator in (2.11) is given by

$$\frac{\partial g}{\partial t} - \lambda \nabla_{\parallel}^6 g + \nabla_{\parallel}^4 g = \delta(x-\xi)\delta(y-\eta)\delta(t), \tag{3.1}$$

subjected to the boundary conditions (2.3) and the initial condition $g(x,y,t=0) = 0$. We employ the finite sine transform with respect to $x$ and $y$ (Miles 1971),

$$G_{n,m}(t) \triangleq \int_0^{l_m} \int_0^{w_m} g(x,y,t) \sin\left(\frac{\pi n x}{l_m}\right) \sin\left(\frac{\pi m y}{w_m}\right) dy dx, \tag{3.2}$$

where the inverse transform is given as (Miles 1971)

$$g(x,y,t) \triangleq \frac{4}{l_m w_m} \sum_{n,\,m=1}^{\infty} G_{n,m}(t) \sin\left(\frac{\pi n x}{l_m}\right) \sin\left(\frac{\pi m y}{w_m}\right). \tag{3.3}$$

Applying the finite sine transform (3.2) on (3.1) and using (2.3) yields

$$\frac{dG_{n,m}(t)}{dt} + F(n,m;\lambda) G_{n,m}(t) = \sin\left(\frac{\pi n \xi}{l_m}\right) \sin\left(\frac{\pi m \eta}{w_m}\right) \delta(t), \tag{3.4}$$

where function $F(n,m;\lambda)$ is

$$F(n,m;\lambda) = \left( \left(\frac{\pi n}{l_m}\right)^2 + \left(\frac{\pi m}{w_m}\right)^2 \right)^2 \left[ \lambda \left( \left(\frac{\pi n}{l_m}\right)^2 + \left(\frac{\pi m}{w_m}\right)^2 \right) + 1 \right]. \tag{3.5}$$

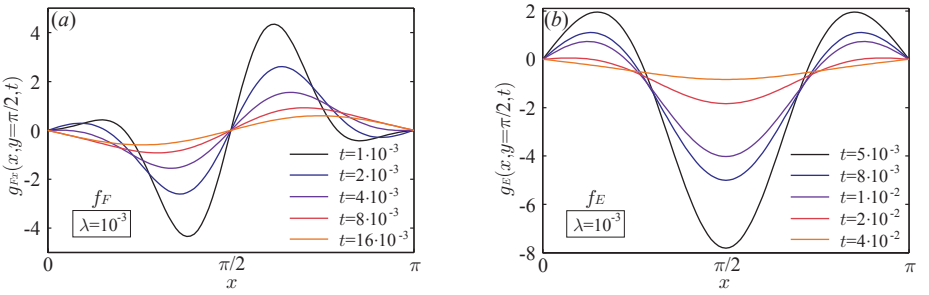


FIGURE 2. Green's functions shapes along the $\hat{\boldsymbol{x}}$ axis for different times, describing the deformation due to an impulse force (3.10) applied at the center of the configuration either (a) through the fluid or (b) directly on the elastic sheet. All calculations were performed using $\lambda = 10^{-3}$ and $l_m = w_m = \pi$.

Solving (3.4) together with initial condition $G_{n,m}(t=0) = 0$, we obtain

$$G_{n,m}(t) = \sin\left(\frac{\pi n\xi}{l_m}\right)\sin\left(\frac{\pi m\eta}{w_m}\right)\mathrm{e}^{-F(n,m;\lambda)t}. \tag{3.6}$$

Substituting (3.6) into (3.3) provides the corresponding Green's function

$$g(x,y,\xi,\eta,t) = \frac{4}{l_m w_m}\sum_{n,\,m=1}^{\infty}\sin\left(\frac{\pi n\xi}{l_m}\right)\sin\left(\frac{\pi m\eta}{w_m}\right)\varphi(x,y,t;n,m), \tag{3.7}$$

where function $\varphi(x,y,t;n,m)$ is given by

$$\varphi(x,y,t;n,m) = \sin\left(\frac{\pi nx}{l_m}\right)\sin\left(\frac{\pi my}{w_m}\right)\mathrm{e}^{-F(n,m;\lambda)t} = \chi(x,y;n,m)\mathrm{e}^{-F(n,m;\lambda)t}. \tag{3.8}$$

The deformation field is thus obtained by convolving Green's function (3.7), yielding

$$d(x,y,t) = \int_0^t\int_\Omega\left(-\boldsymbol{\nabla}_{\xi,\eta}\cdot\boldsymbol{f}_F + \nabla^2_{\xi,\eta}f_E\right)g(x,y,\xi,\eta,t-\tau)d\eta d\xi d\tau. \tag{3.9}$$

To provide more physical insight on the effect of driving forces on the resulting deformations, we further derive an explicit expression for the Green's functions resulting from the impulse force

$$f_{F_x} = f_{F_y} = f_E = \delta(x-\xi_0)\delta(y-\eta_0)\delta(t), \tag{3.10}$$

acting either on the fluid or the elastic plate, where $\delta$ is Dirac's delta function. Substituting (3.10) into (3.9) and using the identity $\int F(y)\delta^{(n)}(y-x)\,dy = (-1)^n F^{(n)}(x)$, yields a general solution for the deformation field explicitly in terms of the external forces

$$d(x,y,t) = \int_0^t\int_\Omega\left(\boldsymbol{f}_F(\xi,\eta,\tau)\cdot\boldsymbol{g}_F(x,y,\xi,\eta,t-\tau) + f_E(\xi,\eta,\tau)g_E(x,y,\xi,\eta,t-\tau)\right)d\eta d\xi d\tau, \tag{3.11}$$

where $\boldsymbol{g}_F = \boldsymbol{\nabla}_{\xi,\eta}g$ and $g_E = \nabla^2_{\xi,\eta}g$. The expressions for $g_{F_x} = \boldsymbol{g}_F\cdot\hat{\boldsymbol{x}}$ and $g_E$ read

$$g_{F_x} = \boldsymbol{\nabla}_{\xi,\eta}\cdot[g\hat{\boldsymbol{x}}] = \frac{4\pi}{l_m^2 w_m}\sum_{n,\,m=1}^{\infty} n\cos\left(\frac{\pi n\xi}{l_m}\right)\sin\left(\frac{\pi m\eta}{w_m}\right)\varphi(x,y,t;n,m), \tag{3.12}$$

$$g_E = -\frac{4\pi^2}{l_m^3 w_m^3}\sum_{n,\,m=1}^{\infty}\left(l_m^2m^2 + w_m^2n^2\right)\sin\left(\frac{\pi n\xi}{l_m}\right)\sin\left(\frac{\pi m\eta}{w_m}\right)\varphi(x,y,t;n,m). \tag{3.13}$$

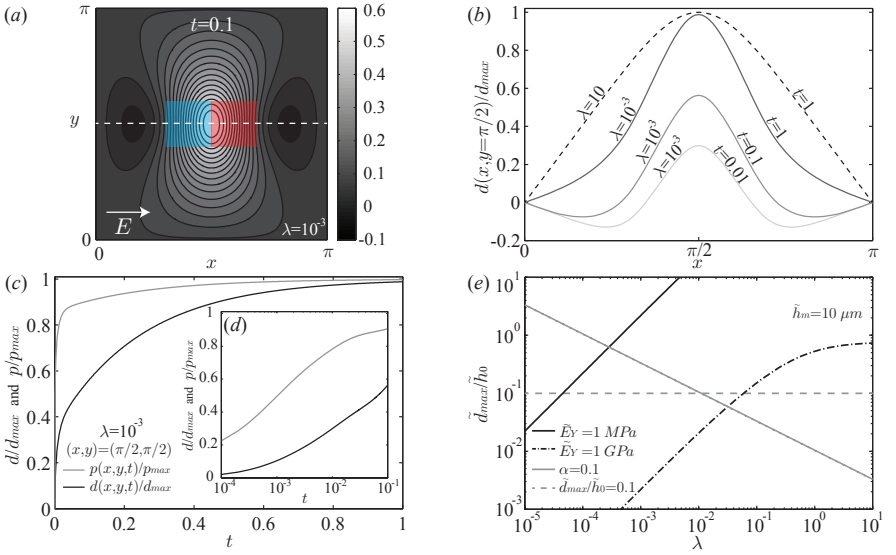


FIGURE 3. Investigation of the deformation field resulting from two square-shaped regions with opposite signs of zeta potential subjected to a constant electric field suddenly applied at $t = 0$. (a) The deformation field (colormap) at $t = 0.1$, superposed on a schematic illustration of the two oppositely directed EOF actuation regions. (b) The scaled steady-state deformation $d/d_{max}$ along the $\hat{\boldsymbol{x}}$, showing the evolution of the deformation for $\lambda = 10^{-3}$, and a comparison between the steady state deformation at $\lambda = 10^{-3}$ (tension dominant) and $\lambda = 10$ (bending dominant). (c-d) The evolution of the maximum deformation and pressure as a function of time. (e) Ratio $\tilde{d}_{max}/\tilde{h}_0$ as a function of $\lambda$, for $\tilde{E}_Y = 1\,\mathrm{MPa}$ and $\tilde{E}_Y = 1\,\mathrm{GPa}$. The dashed and solid gray lines indicate the range of validity of the model where $\tilde{d}_{max}/\tilde{h}_0 = 0.1$ and $\alpha = 0.1$, respectively. All calculations were performed using $\tilde{l} = 5$ mm, $\tilde{h}_0 = 100\,\mu$m, $\tilde{p}^* \approx 1$ Pa, $\tilde{h}_m = 10\,\mu$m, $\nu = 0.5$ $\beta_1 = -\beta_2 = -1$, $\gamma = 0$, $L = \pi/10$ and $\lambda = 10^{-3}$.

Figures 2(a) and 2(b) present the Green's functions (3.12) and (3.13), respectively, representing the deformations resulting from an impulse force (3.10) applied at the center of the elastic sheet, either through the fluid in $\hat{\boldsymbol{x}}$ direction or directly on the elastic sheet in $\hat{\boldsymbol{z}}$ direction.

## 4. Deformations due to a square-shaped actuation region

The general solution given in (3.11) enables to obtain an analytical expression for the deformation field resulting from arbitrary force distributions. Hereafter, we consider the non-uniform Helmholtz-Smoluchowski electro-osmotic slip velocity (Hunter 2000) as a driving force and specifically focus on a square-shaped actuation of the form

$$f(x,y,t) = E(t)\left\{\left[H\left(x-\left(\frac{l_m}{2}+L+\beta L\right)\right)-H\left(x-\left(\frac{l_m}{2}-L+\beta L\right)\right)\right] \times\left[H\left(y-\left(\frac{w_m}{2}+L+\gamma L\right)\right)-H\left(y-\left(\frac{w_m}{2}-L+\gamma L\right)\right)\right]\right\}, \quad (4.1)$$

corresponding to square-shaped zeta potential distribution, where $E(t)$ is a spatially homogeneous and time-dependent electric field along the $\hat{\boldsymbol{x}}$ axis. Here $H$ is the Heaviside function, $L$ is the dimension of the actuation square, and $\beta$ and $\gamma$ indicate the $x$ and $y$ coordinates of its center. For convenience, hereafter we set $l_m = w_m = \pi$.

For a suddenly applied actuation, $E(t) = H(t)$, using (3.11), (3.12) and (4.1), the

resulting deformation is

$$d(x,y,t) = \frac{16}{\pi^2} \sum_{n,\,m=1}^{\infty} \mathcal{A}(n,m;L,\beta,\gamma) \frac{\chi(x,y;n,m)}{mF(n,m;\lambda)} \left(1 - \mathrm{e}^{-F(n,m;\lambda)t}\right), \tag{4.2a}$$

$$\mathcal{A}\,(n,m;L,\beta,\gamma) = \sin(nL)\sin(mL)\sin\left(m(\frac{\pi}{2} + L\gamma)\right)\cos\left(n(\frac{\pi}{2} + L\beta)\right). \tag{4.2b}$$

Figure 3(a) presents the deformation field (4.2*a*) at $t = 0.1$, resulting from two square-shaped regions with opposite signs of zeta potential, subjected to an electric field suddenly applied at $t = 0$, (see also Supplementary Information video 1). The opposing flows result in a positive internal pressure at the interface between the two regions, and negative pressure at the far edges of the squares. Figure 3(b) presents the deformation field (along the $\hat{\boldsymbol{x}}$ axis) as a function of time, for a pre-stretching dominant regime $\lambda = 10^{-3}$. The steady state deformation ($t = 1$) is compared with that obtained for a bending-dominant regime ($\lambda = 10$) showing that the higher order of the dominant term in the bending regime effectively results in additional averaging of the fluidic pressure and thus reduces the spatial resolution of the deformation field. Figures 3(c-d) present the development of the maximum pressure and deformation as a function of time. Importantly, while for a rigid configuration actuation of the electric field would result in an instantaneous jump in pressure (on an acoustic timescale), in the elastic case the evolution of the pressure is coupled to that of the deformation, as given by (2.9). Nevertheless, for the case presented, the rise time to 50% of the final pressure is $t = 10^{-3}$, nearly two orders of magnitude shorter than the viscous-elastic timescale in which the deformation reaches 50% of its steady state value $t = 0.7 \cdot 10^{-1}$. This time delay between pressure and deformation is also evident in periodic actuations (see Supplementary Information video 2) where the deformation phase lags behind that of the pressure. We note that at extremely short timescales, inertial effects must be included to properly describe the deformation dynamics. Figure 3(e) presents the maximal deformation (scaled by $\tilde{h}_0$) as a function of $\lambda$, for a fixed sheet thickness and two different elastic moduli. Consistent with the scaling (2.5) and non-dimensional solution (4.2*a*), as $\lambda$ increases ($\tilde{T}$ decreases), the magnitude of the deformation increases until it reaches a constant value when the problem is dominated entirely by bending. The dashed and solid gray lines respectively indicate the range of validity of the model, where the deformation is no longer small, $\tilde{d}_{max}/\tilde{h}_0 = 0.1$, and where internal stretching is non negligible, $\alpha = 0.1$.

## 5. Effect of pre-stretching on the resolution and magnitude of the deformation field

Aiming to utilize fluidic actuation as a mechanism to create desired deformation in the elastic sheet, it is of interest to examine the tradeoff between the magnitude of deformations and the attainable resolution, for a given amplitude of the actuation force. Any desired deformation can be written as a Fourier series on a finite domain, where the resulting spectrum of frequencies would depend on the desired shape and on its position relative to the boundaries. Consider a steady-state deformation of the form,

$$\tilde{d}\,(\tilde{x},\tilde{y}) = \tilde{d}_0 \sin\left(k_x \pi \frac{\tilde{x}}{\tilde{l}_m}\right) \sin\left(k_y \pi \frac{\tilde{y}}{\tilde{w}_m}\right), \tag{5.1}$$

created due to a non-uniform Helmholtz-Smoluchowski slip velocity, $\tilde{u}_{slip}(\tilde{x},\tilde{y}) = -\tilde{\varepsilon}\tilde{\zeta}(\tilde{x},\tilde{y})\tilde{E}/\tilde{\mu}$, acting in the $\hat{\boldsymbol{x}}$ direction. Here $k_x$ and $k_y$ are wavenumbers in the $\hat{\boldsymbol{x}}$ and $\hat{\boldsymbol{y}}$ directions, respectively, $\tilde{\varepsilon}$ is the fluid permittivity, $\tilde{\zeta}$ is the zeta potential, $\tilde{E}$ is the

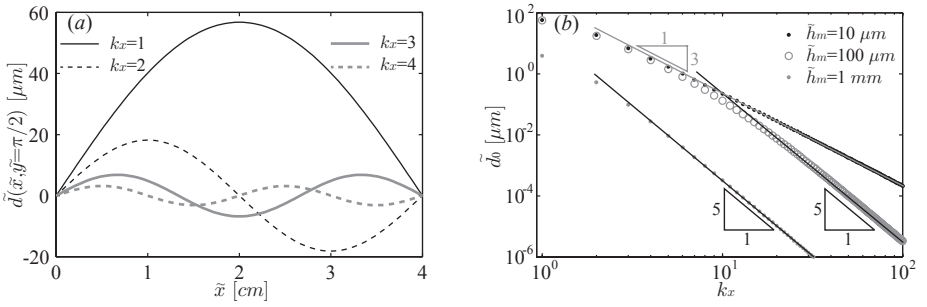


FIGURE 4. The effect of wavenumber on the magnitude of the deformation. (a) Deformation in dimensional form along the $\hat{\boldsymbol{x}}$ axis for various values of $k_x$, $k_y = 1$ and $\tilde{h}_m = 10\ \mu m$. (b) The maximal (dimensional) deformation $\tilde{d}_0$ as a function of wavenumber $k_x$, for $k_y = 1$ and different values of the elastic sheet thicknesses, $\tilde{h}_m$. All calculations were performed using non-uniform electro-osmotic actuation as the driving mechanism, with $\tilde{h}_0 = 30\,\mu m$, $\tilde{l}_m = \tilde{w}_m =$ 4 cm, $\tilde{E}_Y = 0.3$ GPa, $\nu = 0.5$, $\tilde{B} = 3.3 \cdot 10^{-8}$ Pa m$^3$, $\tilde{T} = 1$ Pa m, $\tilde{\zeta}_0 = -70$ mV, $\tilde{E} =$100 V cm$^{-1}$ and $\tilde{\varepsilon} = 7.08 \cdot 10^{-10}$ F m$^{-1}$.

applied electric field, and $\tilde{d}_0$ is the amplitude yet to be determined.
Using (2.12), the zeta potential required for generating the deformation (5.1) is given by

$$\tilde{\zeta}(\tilde{x},\tilde{y}) = \frac{\tilde{h}_0^2}{6\tilde{\varepsilon}\tilde{E}} \int \left(-\tilde{B}\tilde{\nabla}_{\parallel}^6 \tilde{d} + \tilde{T}\tilde{\nabla}_{\parallel}^4 \tilde{d}\right) d\tilde{x} = \tilde{\zeta}_0 \cos\left(k_x \pi \frac{\tilde{x}}{\tilde{l}_m}\right) \sin\left(k_y \pi \frac{\tilde{y}}{\tilde{w}_m}\right), \tag{5.2}$$

enabling to explicitly express the amplitude $\tilde{d}_0$ in terms of relevant physical quantities,

$$\tilde{d}_0 = 6\frac{\tilde{\varepsilon}\left|\tilde{\zeta}_0\right|\tilde{E}}{\pi^3 \tilde{h}_0^2} \frac{\tilde{l}_m^5 \tilde{w}_m^6 k_x}{\left(\tilde{l}_m^2 k_y^2 + \tilde{w}_m^2 k_x^2\right)^2 \left(\pi^2 \tilde{B}\left(\tilde{l}_m^2 k_y^2 + \tilde{w}_m^2 k_x^2\right) + \tilde{T}\tilde{l}_m^2 \tilde{w}_m^2\right)}. \tag{5.3}$$

Using the physical values noted in its caption, figure 4(a) presents the resulting deformation (5.1) along the $\hat{\boldsymbol{x}}$ axis for various values of $k_x$, for $k_y = 1$ and $\tilde{h}_m = 10\mu m$, and clearly shows the reduction in deformation magnitude as the wavenumber increases. Furthermore, (5.3) indicates that the scaling of the deformation with the wavenumber depends on the relative contribution of the bending and tension terms in the denominator. When $\pi^2 \tilde{B} k_x^2 \ll \tilde{T}\tilde{l}_m^2$, pre-stretching is dominant over bending forces and the deformation $\tilde{d}_0$ scales as $k_x^{-3}$. However, when $\pi^2 \tilde{B} k_x^2 \gg \tilde{T}\tilde{l}_m^2$, bending is dominant and the deformation scales as $k_x^{-5}$. From the definition of $\tilde{B}$, the conditions for pre-stretching dominance can be expressed as $\pi^2 \tilde{E}_Y \tilde{h}_m^3 k_x^2 / 12(1-\nu^2)\tilde{T}\tilde{l}_m^2 \ll 1$. Figure 4(b) presents the maximum deformation as a function of $k_x$ for three values of the membrane thickness, $\tilde{h}_m$, showing that the deformation of a 10 $\mu m$ thick sheet scales as $k_x^{-3}$ throughout the investigated range, whereas for $\tilde{h}_m = 100\ \mu m$ it scales as $k_x^{-3}$ for sufficiently low $k_x$ values, but settles on a $k_x^{-5}$ dependence for high wavenumbers.

## 6. Effect of discretized actuation on the deformation field

Equation (2.11) may be solved to obtain the actuation field required to achieve predefined deformation patterns of elastic plates, which may be desired in engineering applications. However, implementation of the resulting continuous zeta potential distribution may be challenging in practice. We therefore discretize the continuous zeta potential into individual squares hosting mean values of zeta potential, better representing more realistic actuation (e.g. finite gate electrodes), and examine the effect

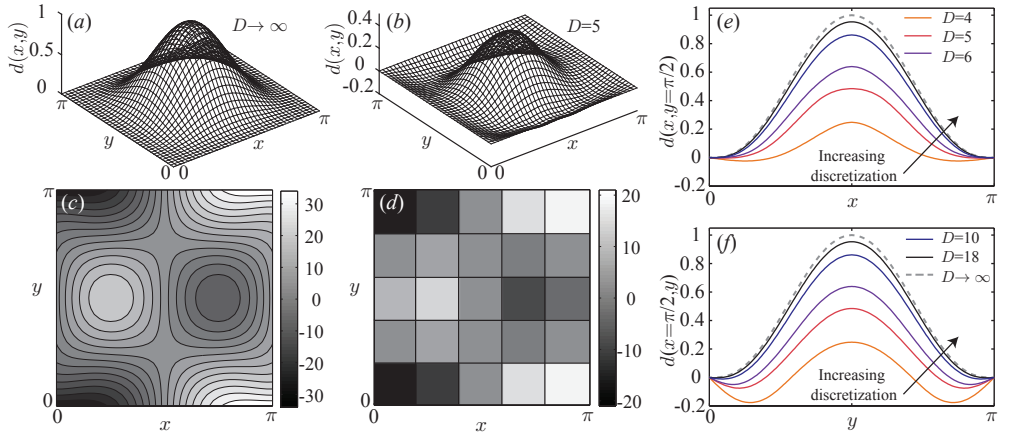


FIGURE 5. The effect of actuation discretization on the shape and the magnitude of the deformation. (a) Deformation formed by the continuous zeta potential shown in (c), for an electric field acting in the $\hat{\boldsymbol{x}}$ direction. (b) Deformations obtained from discretization of the zeta potential field into 5x5 squares, each having a mean zeta value as shown in (d). (e-f) Deformation along the $\hat{\boldsymbol{x}}$ and $\hat{\boldsymbol{y}}$ axes, respectively, for different levels of discretization.

of such discretization on the resulting deformations. As a test case, we consider a localized deformation, $d(x,y) = (2/\pi)^{12} x^3 (x-\pi)^3 y^3 (y-\pi)^3$ shown in figure 5(a), and for simplicity assume a membrane regime (dominant pre-stretching, $\lambda = 0$). For an electric field $E$ directed along the $\hat{\boldsymbol{x}}$ axis, we use (2.11) to express the zeta potential required to form this deformation (at steady-state),

$$\zeta(x,y) = -\frac{1}{E}\int (\nabla_{\parallel}^4 d(x,y))dx + \zeta_0(y), \tag{6.1}$$

as shown in figure 5(c). We choose the function $\zeta_0(y)$ such that $\zeta(x,y)$ is anti-symmetric with respect to the centerline $x = \pi/2$. Figure 5(d) shows the discretization of this field into 5x5 square-shaped regions, each assigned with a uniform zeta potential value equal to the mean value of $\zeta(x,y)$ over its surface. Figure 5(b) presents the resulting deformation obtained by superposition of solutions for individual squares (4.2*a*). Figures 5(e-f) present the deformation along the $\hat{\boldsymbol{x}}$ and $\hat{\boldsymbol{y}}$ axes, respectively, for different levels of discretization. While, as expected, discretization results in undesired oscillations of the deformation field due to high wavenumbers which are unbalanced, even a relatively coarse discretization (e.g. $D = 5$) allows to maintain a fairly localized deformation, though with a clearly reduced amplitude. For $D = 10$, the resulting amplitude is approximately 86% of the desired one, with a negative deformation value that is less than 1.2% of the peak.

## 7. Concluding remarks

We examined the effect of pre-stretching and finite boundaries on the deformation dynamics of an elastic sheet lying on top of a thin liquid film. The Green's functions we derived allow to obtain closed-form solutions for realistic configurations and to study the tradeoff between deformation amplitude and resolution as well as examine spatially discretized actuation. These results can be directly applied to implementation of actuators making use of lubricated elastic sheets.

While our main focus was on actuations applied to the fluid (specifically by non-uniform slip velocity), the Green's function (3.12) can be readily utilized to investigate the viscous-elastic dynamics due to forces applied directly on the solid sheet. For such

actuation, as shown by (2.9), the pressure in the fluid can be described solely by the temporal variation of the deformation field, returning to zero gauge pressure as the deformation reaches steady-state. This is in contrast to the case of forcing applied to the fluid, where the pressure field is described by the contributions of both the temporal variation of the deformation and the external forcing.

Finally, while the current study focused on strong pre-stretching, from a practical perspective it is preferable to minimize pre-stretching to maximize the amplitude of the deformations. In fact, negative pre-stretching (compression) may allow to further increase the amplitude, provided that the compressive force is below the critical value of the buckling instability.

## REFERENCES


Al-Housseiny, T. T., Christov, I. C. & Stone, H. A. 2013 Two-phase fluid displacement and interfacial instabilities under elastic membranes. *Phys. Rev. Lett.* **111** (3), 034502.

Arutkin, M., Ledesma-Alonso, R., Salez, T. & Raphaël, E. 2016 Elastohydrodynamic wake and wave resistance. *arXiv:1607.07816* .

Chronis, N., Liu, G. L., Jeong, K. H. & Lee, L. P. 2003 Tunable liquid-filled microlens array integrated with microfluidic network. *Opt. express* **11** (19), 2370–2378.

Grotberg, J. B. & Jensen, O. E. 2004 Biofluid mechanics in flexible tubes. *Annu. Rev. Fluid Mech.* **36**, 121–147.

Hewitt, I. J., Balmforth, N. J. & De Bruyn, J. R. 2015 Elastic-plated gravity currents. *Eur. J. Appl. Maths* **26** (01), 1–31.

Hosoi, A. E. & Mahadevan, L. 2004 Peeling, healing, and bursting in a lubricated elastic sheet. *Phys. Rev. Lett.* **93** (13), 137802.

Howell, P., Kozyreff, G. & Ockendon, J. 2009 *Applied solid mechanics*. Cambridge University Press.

Hunter, R. J. 2000 *Foundations of colloid science*. Oxford University Press.

Kim, S., Laschi, C. & Trimmer, B. 2013 Soft robotics: a bioinspired evolution in robotics. *Trends Biotechnol.* **31** (5), 287–294.

Kodio, O., Griffiths, I. M. & Vella, D. 2017 Lubricated wrinkles: Imposed constraints affect the dynamics of wrinkle coarsening. *Phys. Rev. Fluids* **2** (1), 014202.

Leal, L. G. 2007 *Advanced Transport Phenomena: Fluid Mechanics and Convective Transport Processes*. Cambridge University Press.

Lister, J. R., Peng, G. G. & Neufeld, J. A. 2013 Viscous control of peeling an elastic sheet by bending and pulling. *Phys. Rev. Lett.* **111** (15), 154501.

Michaut, C. 2011 Dynamics of magmatic intrusions in the upper crust: Theory and applications to laccoliths on earth and the moon. *J. Geophys. Res.* **116** (B5).

Miles, J. W. 1971 *Integral transforms in applied mathematics*. Cambridge University Press.

Pihler-Puzović, D., Illien, P., Heil, M. & Juel, A. 2012 Suppression of complex fingerlike patterns at the interface between air and a viscous fluid by elastic membranes. *Phys. Rev. Lett.* **108** (7), 074502.

Pihler-Puzović, D., Juel, A. & Heil, M. 2014 The interaction between viscous fingering and wrinkling in elastic-walled Hele-Shaw cells. *Phys. Fluids* **26** (2), 022102.

Pihler-Puzović, D., Périllat, R., Russell, M., Juel, A. & Heil, M. 2013 Modelling the suppression of viscous fingering in elastic-walled Hele-Shaw cells. *J. Fluid Mech.* **731**, 162–183.

Rubin, S., Tulchinky, A., Gat, A. D. & Bercovici, M. 2017 Elastic deformations driven by non-uniform lubrication flows. *J. Fluid Mech.* **812**, 841–865.

Timoshenko, S. & Woinkowsky-Krieger, S. 1987 *Theory of Plates and Shells,(1987)*. McGraw-Hill, New York.

Tulchinsky, A. & Gat, A. D. 2016 Transient dynamics of an elastic Hele-Shaw cell due to external forces with application to impactmitigation. *J. Fluid Mech.* **800**, 517–530.

Whitesides, G. M., Ostuni, E., Takayama, S., Jiang, X. & Ingber, D. E. 2001 Soft lithography in biology and biochemistry. *Annu. Rev. Biomed. Eng.* **3** (1), 335–373.